

Gate-Tunable Transport in Quasi-One-Dimensional α -Bi₄I₄ Field Effect Transistors

Yulu Liu, Ruoyu Chen, Zheneng Zhang, Marc Bockrath, Chun Ning Lau,* Yan-Feng Zhou, Chiho Yoon, Sheng Li, Xiaoyuan Liu, Nikhil Dhale, Bing Lv,* Fan Zhang,* Kenji Watanabe, Takashi Taniguchi, Jianwei Huang, Ming Yi,* Ji Seop Oh, and Robert J. Birgeneau*



Cite This: <https://doi.org/10.1021/acs.nanolett.1c04264>



Read Online

ACCESS |



Metrics & More



Article Recommendations

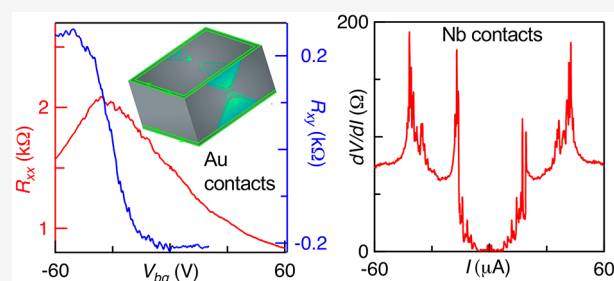


Supporting Information

ABSTRACT: Bi₄I₄ belongs to a novel family of quasi-one-dimensional (1D) topological insulators (TIs). While its β phase was demonstrated to be a prototypical weak TI, the α phase, long thought to be a trivial insulator, was recently predicted to be a rare higher order TI. Here, we report the first gate tunable transport together with evidence for unconventional band topology in exfoliated α -Bi₄I₄ field effect transistors. We observe a Dirac-like longitudinal resistance peak and a sign change in the Hall resistance; their temperature dependences suggest competing transport mechanisms: a hole-doped insulating bulk and one or more gate-tunable ambipolar boundary channels. Our combined transport, photoemission, and theoretical

results indicate that the gate-tunable channels likely arise from novel gapped side surface states, two-dimensional (2D) TI in the bottommost layer, and/or helical hinge states of the upper layers. Markedly, a gate-tunable supercurrent is observed in an α -Bi₄I₄ Josephson junction, underscoring the potential of these boundary channels to mediate topological superconductivity.

KEYWORDS: quasi-1D topological insulator, Bi₄X₄, Josephson transistor, topological superconductivity



Topological insulators (TIs) are insulating in the bulk yet conducting on the boundary, protected by symmetry and immune to disorder.^{1,2} They enable near-perfect devices using imperfect interfaces for breakthrough technologies. Their discovery has led to an ongoing revolution, deepening our fundamental understanding in condensed matter and materials physics. Over the past decade, there has been rapidly growing interest in the search for TI materials.^{3–11} Thus far, most of them are either three-dimensional (3D) strongly bonded bulk materials in the first generation, e.g., Bi_{1–x}Sb_x alloys with rather complicated surfaces states,^{12,13} or quasi-two-dimensional (2D)-layered van der Waals materials in the second generation, e.g., the Bi₂Se₃ family compounds with only one surface Dirac cone.^{14–16} Recently, for the search of the rare weak TIs, first-principles calculations predicted a new generation of TI materials Bi₄I₄ and Bi₄Br₄ in a quasi-one-dimensional (1D) geometry, which uniquely harbor two natural cleavage surfaces and feature two Dirac cones at only one of the cleavage surfaces.³ They promise several advantages, such as multiple cleavage planes, strain-induced phase transitions between weak TI, strong TI, and trivial insulator states, and hosting of prototypical higher order TIs with helical hinge modes.^{3–8} As shown in Figure 1a, Bi₄I₄ is composed of a periodic stack of atomic chains aligned in the *b* direction,^{17–19} with very weak interlayer binding energies for the (100) and (001) planes.^{3,17} In each unit cell, the two internal Bi atoms form zigzag chains,

while the two external Bi atoms are each bonded to four I atoms and one internal Bi atom. The crystals have two independent symmetries: spatial inversion and (010) mirror reflection.

Bi₄I₄ has two structural phases, α and β , which crystallize in the same space group *C2/m* yet mainly⁶ differ in the way their (001) monolayers are stacked.^{17–19} In Bi₄I₄, an important structural phase transition at \sim 300 K between the two phases has been observed.^{5,7,20} More notably, the weakly coupled Bi₄I₄ (001) monolayers are 2D TIs⁶ (Figure 1d), although each monolayer may relax into a trivial insulator when freestanding.²¹ Recently, the high-temperature phase, β -Bi₄I₄, has been confirmed by angle-resolved photoemission spectroscopy (ARPES)^{4,5,7} to be a weak TI, whereas the low-temperature phase α -Bi₄I₄ has long been thought to be a trivial insulator, even using the state-of-the-art classification tools.^{3,21–24} However, a more recent theoretical investigation predicts that α -Bi₄I₄ is a rare higher order TI⁶ that hosts an

Received: November 5, 2021

Revised: January 14, 2022

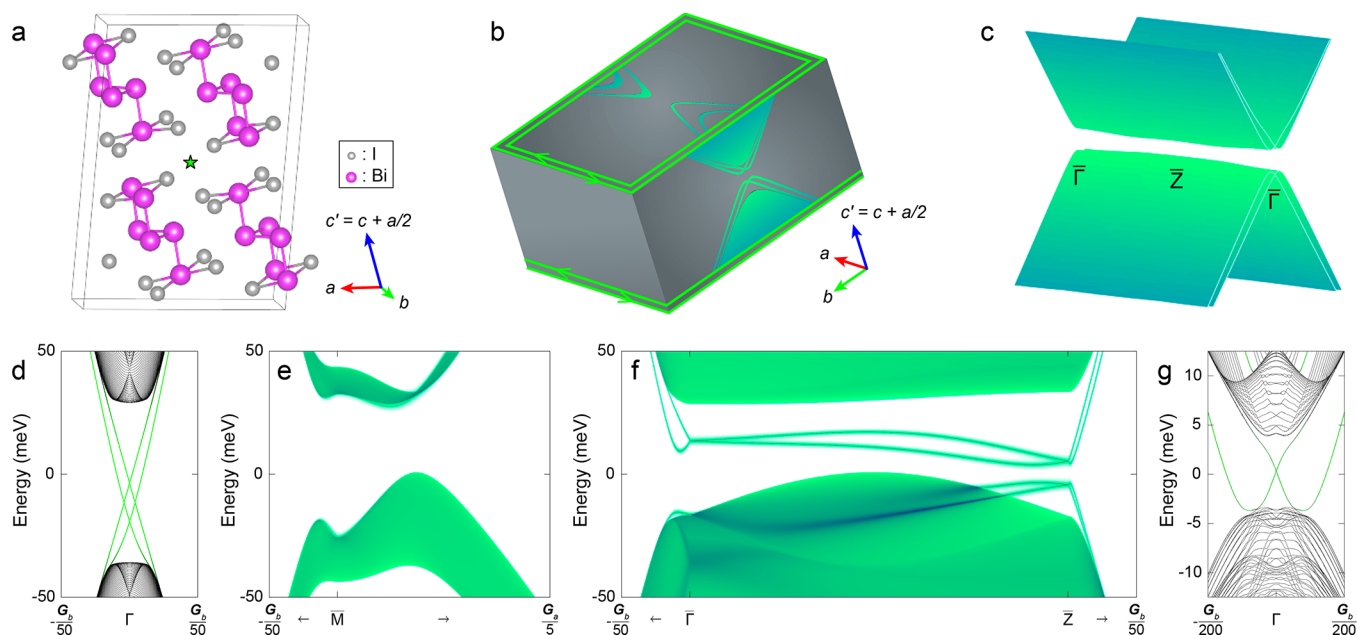


Figure 1. Band structure and characterization of bulk Bi_4I_4 crystals. (a) Crystal structure of $\alpha\text{-Bi}_4\text{I}_4$. The gray box and green star are the conventional unit cell and inversion center, respectively. (b) Schematic of the higher order TI state of $\alpha\text{-Bi}_4\text{I}_4$ with a particular surface termination. The bulk and surface bands are all gapped, and a helical hinge state around the top/bottom surface exists in the surface-state gap. (c) Zoom-in (100) side surface state in panel b featuring double Dirac cones with a small gap in the chain direction and a nearly vanishing dispersion in the stacking direction. (d) Edge-projected band structure of monolayer $\alpha\text{-Bi}_4\text{I}_4$. The green lines are the helical edge states at two parallel edges. (e) (001) surface-projected band structure of bulk $\alpha\text{-Bi}_4\text{I}_4$. No surface states exist in the bulk gap. (f) (100) surface-projected band structure of bulk $\alpha\text{-Bi}_4\text{I}_4$. The green lines are the (100) side surface state in panel c. (g) Hinge-projected band structure of bulk $\alpha\text{-Bi}_4\text{I}_4$. The green lines are the hinge states along the chain direction in panel b, and the black lines are the (100) and $(\bar{1}00)$ side surface states. Note that G_a and G_b are the reciprocal lattice vectors using the conventional unit cell notation and that the Miller indices are named using the a - b - c' notation. See the Supporting Information for computational details.

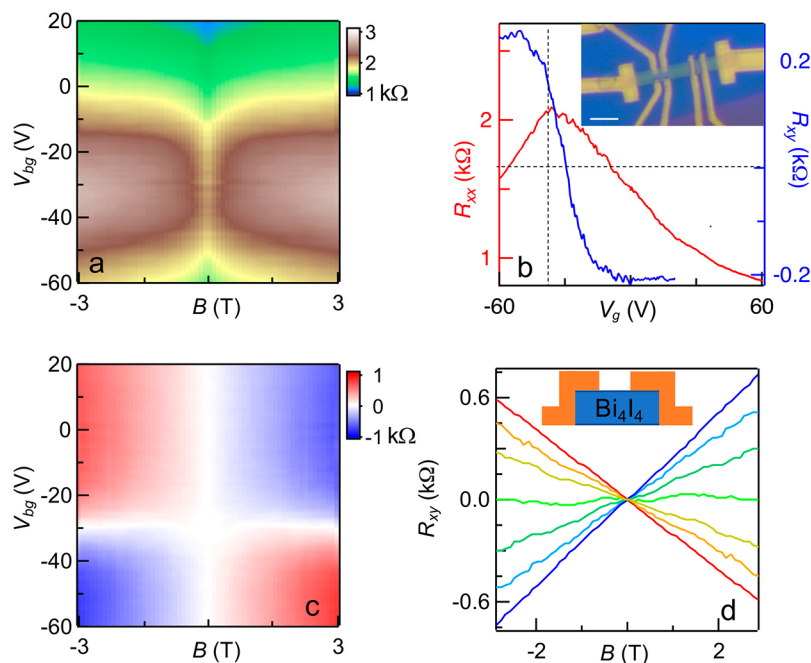


Figure 2. Magneto-transport data from device D1. (a) $R_{xx}(V_g, B)$ at $T = 1.8$ K. (b) $R_{xx}(V_{bg})$ at $B = 0$ and $R_{xy}(V_{bg})$ at $B = 1$ T. (Inset) Optical image of a device. Scale bar = $5 \mu\text{m}$. (c) $R_{xy}(V_g, B)$ at $T = 2$ K. (d) $R_{xy}(B)$ at $T = 1.7$ K for $V_g = 20, -20, -25, -30, -35, -40,$ and -60 V, respectively. (Inset) Schematic of the side view of device contacts (orange).

65 insulating bulk state and gapped surface states (panels b, c, e,
66 and f of Figure 1) yet gapless hinge states (panels b and g of
67 Figure 1), which may be viewed as the time-reversal-invariant
68 counterpart of the long-desired 3D quantum Hall effect^{25,26} or

the 3D counterpart of the celebrated Su–Schrieffer–Heeger⁶⁹
69 model.²⁷

Despite the rising interest in quasi-1D TIs in the community⁷¹
71 and the alluring prospects of Bi_4I_4 , all experiments to date have⁷²

73 been performed on bulk materials.^{4,5,7,18,28–31} However, to
 74 ultimately demonstrate the presence of non-trivial surface and
 75 hinge states and to leverage the room-temperature topological
 76 phase transition in Bi₄I₄ as the topological switch between 2D
 77 surface and 1D hinge conduction, a demonstration of gate-
 78 tunable transport is of paramount importance. Here, we seek
 79 to explore the electronic properties of Bi₄I₄ thin-film
 80 transistors. Bulk crystals are grown by the chemical vapor
 81 transport method. Although the β phase may be obtained at a
 82 low temperature via rapid quenching at high temperatures,⁵
 83 crystals that are cooled slowly from room temperature are
 84 observed to be in the α phase.⁷

85 We fabricate thin-film Bi₄I₄ field effect transistors, which are
 86 encapsulated by hexagonal BN (hBN) (see the Supporting
 87 Information for details of crystal growth and characterization,
 88 device fabrication, and computation techniques). An optical
 89 image of a Bi₄I₄ device D1 is illustrated in the inset of Figure
 90 2b, and the schematic of the device side view is shown in the
 91 inset of Figure 2d. The surface of the exfoliated sheet is the a -
 92 b plane, and the c axis is the out-of-plane direction. Panels a–c
 93 of Figure 2 display the longitudinal resistivity R_{xx} and Hall
 94 resistivity R_{xy} of device D1, which is ~ 25 nm thick, as a
 95 function of the gate voltage V_g and magnetic field B at
 96 temperature $T = 1.8$ K. The R_{xy} data are antisymmetrized with
 97 respect to B to remove artifacts induced by, e.g., slight
 98 misalignment between the Hall voltage probes. Transport is
 99 performed along the b axis, i.e., the atomic chain direction.
 100 Interestingly, both resistances are strongly gate-dependent. For
 101 instance, at $B = 0$, as the gate voltage increases from $V_g = -60$
 102 V, R_{xx} increases until it reaches a peak of ~ 2 k Ω at $V_{g,max} =$
 103 -36.5 V; for $V_g > V_{g,max}$ R_{xx} continuously decreases and lowers
 104 to ~ 0.8 k Ω at $V_g = 60$ V (red curve and left axis of Figure 2b).
 105 This prominent R_{xx} peak in gate modulation is similar to those
 106 observed in Dirac materials, such as graphene,³² 2D TIs, such
 107 as HgTe and InAs/GaSb quantum wells,^{33,34} and the surface
 108 states of 3D TIs, such as Bi₂Se₃,^{35,36} and suggests the presence
 109 of a Dirac point or a very small band gap ($k_B T \sim 0.15$ meV,
 110 where k_B is Boltzmann's constant); hence, we refer to the peak
 111 as “Dirac-like”. Similarly, R_{xy} is strongly gate-tunable, becoming
 112 negative for $V_g \gg V_{g,max}$ and positive for $V_g \ll V_{g,max}$ indicating
 113 hole- and electron-dominated transport, respectively (blue
 114 curve and right axis of Figure 2b). For the entire range of gate
 115 voltage studied, R_{xy} is linear in B , as expected from the Drude
 116 model (Figure 2d). Thus, the strong gate dependence of R_{xx}
 117 and R_{xy} , together with the sign change in the latter,
 118 unambiguously establishes the presence of a gate-tunable
 119 channel in α -Bi₄I₄ transistors.

120 On the other hand, if the gate-tunable channel is the only
 121 conduction channel, we would expect that R_{xy} scales as $1/(ne)$,
 122 where n is the charge carrier density and e is the electron
 123 charge. Thus, R_{xy} should rapidly decrease once V_g is tuned past
 124 the Dirac-like peak in R_{xx} . However, in Figure 2b, for an
 125 extended range $V_g > V_{g,max}$ R_{xy} remains almost constant, while
 126 R_{xx} steadily decreases; these behaviors are inconsistent with a
 127 single-carrier Drude model. To gain further insight into the
 128 transport properties of Bi₄I₄, we investigate the evolution of
 129 $\rho_{xx}(V_g)$ at $B = 0$ with the temperature for device D2, which is
 130 ~ 45 nm thick (Figure 3a). Here, transport is performed along
 131 the a axis. Similar to device D1, R_{xx} is gate-tunable, with a
 132 resistivity peak at $V_{g,max} \sim -48$ V. The collection of $R_{xx}(V_g)$
 133 curves taken at different temperatures, shown in the inset of
 134 Figure 3b, appears to cross at a single point, $V_g = -6$ V and R_{xx}
 135 $= 2$ k Ω ; for $V_g < -6$ V ($V_g > -6$ V), R decreases (increases)

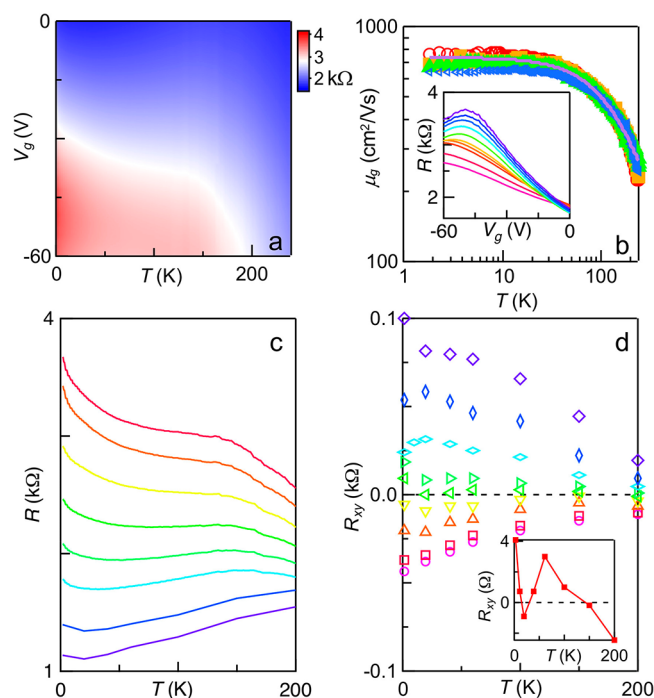


Figure 3. Temperature-dependent data from device D2. (a) $R_{xx}(V_g, T)$ in k Ω taken at $B = 0$. (b) Mobility of the gate-tunable state, calculated using eq 1. The data sets are taken at $(V_{g1}, V_{g2}) = (0, -5$ V), $(-5, -10$ V), $(-10, -15)$, and $(-15, -20$ V), respectively. The solid line is a fit to $\mu_0/(1 + (T/A)^\alpha)$, yielding $\alpha = 1.5$ and $\mu_0 \sim 730$ cm² V⁻¹ s⁻¹. (Inset) $R_{xx}(V_g)$ at $T = 2, 5, 10, 20, 40, 80, 120, 150, 180,$ and 200 K, respectively (from top to bottom). (c) $R_{xx}(T)$ at $V_g = -60, -40, -30, -20, -10, 0, 20,$ and 40 V, respectively (from top to bottom). (d) $R_{xy}(T)$ at $B = 1$ T and $V_g = -60, -40, -30, -20, -15, -10, 0, 20,$ and 40 V (from top to bottom). (Inset) $R_{xy}(T)$ at $V_g = -14$ V, showing multiple sign changes as T decreases. R_{xx} and R_{xy} data are symmetrized and antisymmetrized with respect to B , respectively.

with increasing temperature, indicating insulating (metallic) transport. This metal–insulator transition-like behavior, driven by the gate voltage, is more clearly seen in Figure 3c, where $R_{xx}(T)$ is plotted at different gate voltages. When the device is highly doped ($V_g > 0$), $dR_{xx}/dT > 0$ for most of the temperature range, except for a small resistivity uptick at $T < 30$ K, suggesting a largely metallic regime. In contrast, when the device is close to the resistivity peak, $dR_{xx}/dT < 0$ for the entire temperature range; the slope of the curve is steep near $T \sim 200$ K, becoming almost flat between 135 and 75 K, and picks up again at low temperatures, $T < 50$ K. Such variations in the slopes of the $R_{xx}(T)$ curves suggest the presence of more than one transport mechanism. Another clue is given by the $R_{xy}(T)$ curves at $B = 1$ T for different gate voltages (Figure 3d), which are positive for $V_g \sim V_{g,max}$ indicating hole-dominated transport, and negative for $V_g \gg V_{g,max}$. Taken together, we conclude that there are two competing transport mechanisms: an insulator-like bulk state that is hole-doped and an ambipolar metallic boundary state that can be tuned by V_g .

We note that the co-existence of bulk and boundary states can successfully account for the puzzlingly large variations in the temperature dependence of the resistance in bulk Bi₄I₄ devices reported to date;^{5,29,30} because the boundary state is sensitive to charge transfer, the variations in temperature dependence can be attributed to different doping levels of the boundary charges induced by, e.g., contaminants. Moreover, our data are also consistent with the observed multiple sign

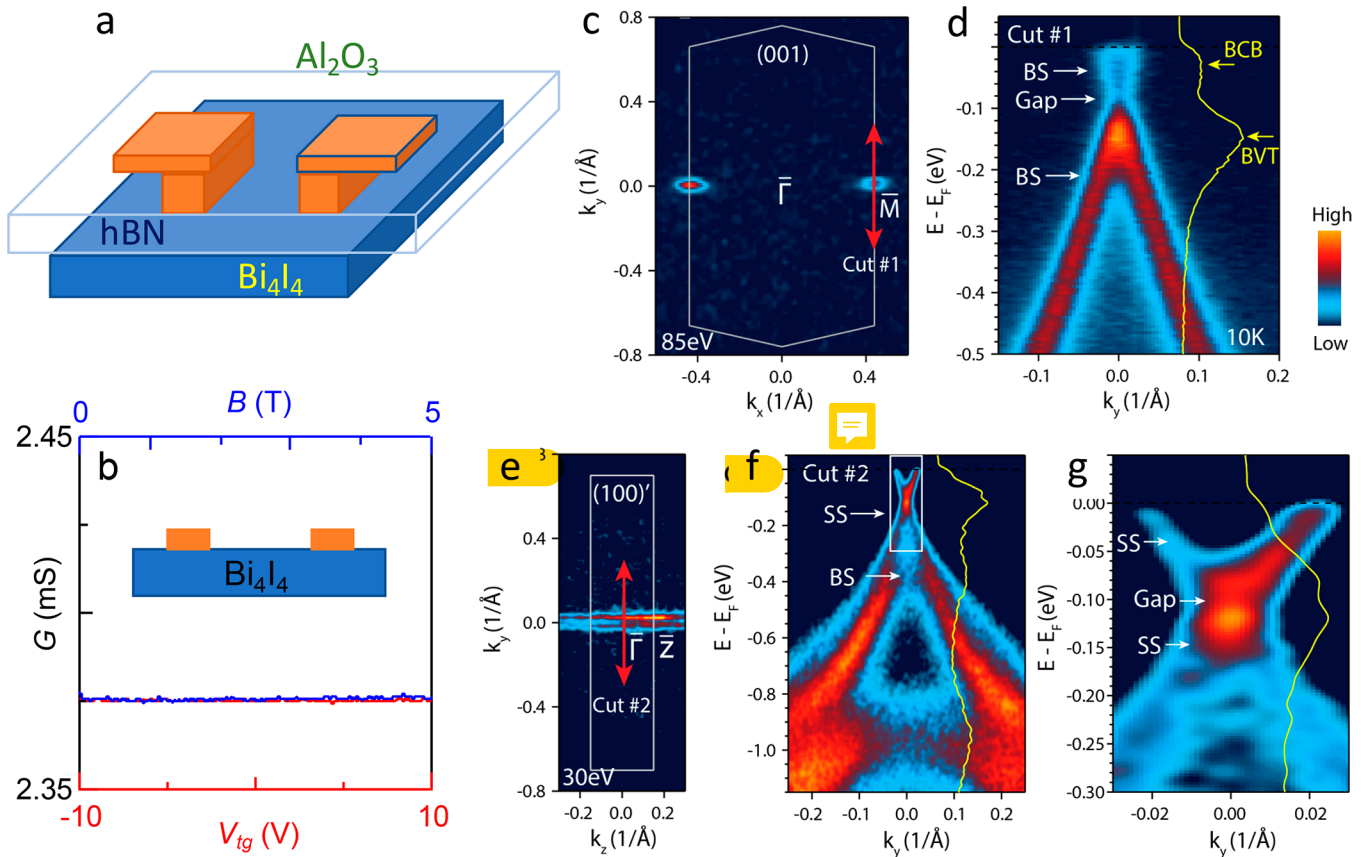


Figure 4. Transport and ARPES data excluding surface states on the a - b plane. (a) Schematic of a bulk-contacted device with top gate dielectric Al_2O_3 and top gate (not shown). (b) Two-terminal conductance of a bulk-contacted device versus top gate voltage (bottom axis) and B (top axis). (Inset) Schematic of the side view of the device contacts. (c) Fermi surface mapping of α - Bi_4I_4 on the (001) top surface measured at 10 K with 85 eV photon energy. The gray frame represents the surface Brillouin zone. (d) Band image of cut 1 indicated in panel c. The white arrows mark the related bulk state (BS) and bulk band gap. The solid yellow line represents the energy distribution curve at $k = 0$. Related bulk valence band top (BVT) and bulk conduction band bottom (BCB) are marked by the yellow arrows. (e and f) Same as panels c and d but measured on the (100)' side surface. The photon energy was set to 30 eV to better resolve the surface states (SS). The yellow arrows point to the surface valence band top (SVT) and surface conduction band bottom (SCB). (g) Zoom-in image of the boxed area in panel f. The yellow arrows point to the surface valence band top (SVT) and surface conduction band bottom (SCB), identifying a gap in the surface state.

163 changes in the $R_{xy}(T)$ curve in one report;²⁹ if the device is
 164 nearly compensated, the competition between the hole-doped
 165 insulator-like bulk state and the electron-doped metallic
 166 boundary state results in sign changes as T is lowered. Indeed,
 167 this is observed in device D2 at $V_g = -14$ V (inset of Figure
 168 3d), where ρ_{xy} is negative at high and low temperatures yet
 169 positive at intermediate temperatures.

170 To delineate further bulk and boundary transport, we model
 171 the device conductivity by $\sigma(V_g, T) = \sigma_g(V_g, T) + \sigma_b(T)$, where
 172 σ_b and σ_g are conductivities of the bulk and gate-tunable
 173 channels, respectively. Because $\sigma_b(T)$ is a constant at a given
 174 temperature, mobility of the gate-tunable channel can be
 175 extracted from the difference in total conductivity at different
 176 gate voltages

$$177 \mu_g(T) = \frac{\sigma(V_{g1}, T) - \sigma(V_{g2}, T)}{C_g(V_{g1} - V_{g2})} \quad (1)$$

178 where C_g is the capacitance between the gate and the boundary
 179 state. Using an estimated $C_g \sim 11.8$ nF/cm² for parallel plate
 180 capacitance between the flake and the Si back gate, we
 181 calculate $\mu_g(T)$ from three different pairs of (V_{g1}, V_{g2}) traces
 182 (Figure 3b). These curves collapse into a single trace,
 183 indicating that μ_g is approximately independent of charge

184 density. Because μ_g has a power law scaling with the
 185 temperature for phonon-dominated scattering at a high
 186 temperature and is nearly a constant for disorder-dominated
 187 scattering at a low temperature, we fit the curves to $\mu_g = \mu_0 / (1 + (T/A)^\alpha)$,
 188 where μ_0 and A are fitting parameters. With $\alpha = 1.5$
 189 and $\mu_0 \sim 730$ cm² V⁻¹ s⁻¹, the fits are in excellent agreement
 190 with data and consistent with phonon-dominated scattering for
 191 $T > \sim 150$ K.

To summarize our observations thus far: (i) There is one or
 192 more gate-tunable transport channels in α - Bi_4I_4 . (ii) Transport
 193 through these channel(s) contribute to both longitudinal and
 194 Hall conductances. (iii) This channel is metallic and
 195 ambipolar, thus hosting either a Dirac point or a very small
 196 band gap. What is the origin of this gate-tunable state? A trivial
 197 mechanism is that it arises from a bulk band, which is lightly
 198 doped, so that charge density in the few bottommost layers is
 199 tuned by the back gate, while that deep in the bulk remains
 200 undisturbed as a result of screening. Alternatively, it originates
 201 from the top/bottom surface states on the a - b plane. To
 202 examine these possibilities, we note that these scenarios
 203 necessitate a top layer (or a few top layers) that conducts
 204 current uniformly. Thus, we fabricate a device with pre-
 205 patterned holes on the top hBN layer, so that contacts are only
 206 made to the interior (as opposed to the edge) of the top
 207

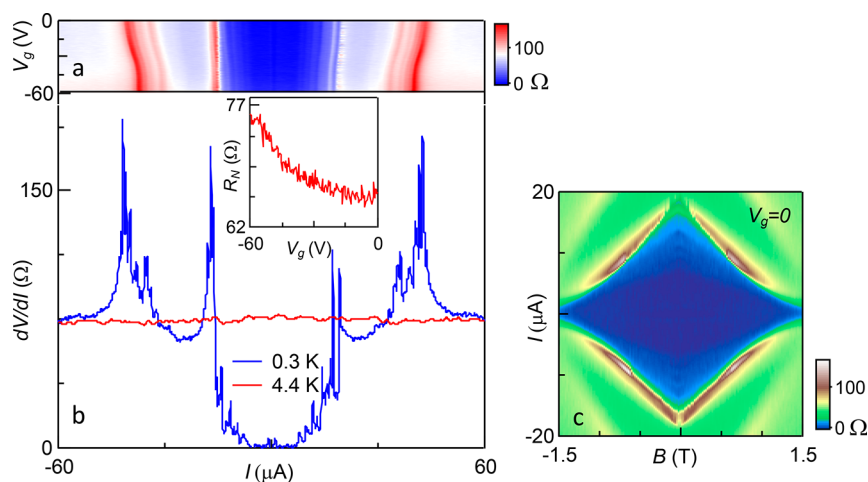


Figure 5. Supercurrent in a Bi_4I_4 Josephson junction. (a) Differential resistance dV/dI in unit of Ω versus bias current I and V_g . The dark blue region signifies the supercurrent. (b) dV/dI at $V_g = 0$ and $T = 0.3$ and 4.4 K, respectively. (Inset) Normal state resistance $R_N(V_g)$. (c) dV/dI in unit of Ω versus I and B at $V_g = 0$, where B is perpendicular to the a - b plane.

208 surface of a Bi_4I_4 flake that is ~ 25 nm in thickness. The device
 209 is completed by depositing Al_2O_3 and a metal top gate. A
 210 schematic of this device is shown in Figure 4a. Resistance of
 211 such a device is ~ 2 k Ω , indicating a conductive bulk and/or a
 212 conductive top surface. Here, the resistance is completely
 213 independent of the back gate voltage, top gate voltage, and
 214 magnetic field (Figure 4b), in sharp contrast to the data in
 215 Figures 2 and 3. This difference arises from regions at which
 216 the contacts are made: here, the contacts are made on the
 217 interior of the top surface (see the inset of Figure 4b), whereas
 218 contacts in the “standard” devices in Figures 2 and 3 cover
 219 both the interior and the edges (see the inset of Figure 2d).
 220 The gate independence of the interior-contacted device
 221 therefore excludes the bulk band and the top surface state as
 222 the origin of the gate-tunable channel; given the similarity of
 223 the top and bottom surface states, we also exclude the bottom
 224 surface state. The absence of surface states on the a - b plane is
 225 in fact consistent with first-principles calculations³ (Figure 1e)
 226 and further verified by ARPES measurements on bulk crystals,
 227 as shown in panels c and d of Figure 4. There is no discernible
 228 surface state on the (001) a - b plane of α - Bi_4I_4 , where only a
 229 gapped bulk state is observed by ARPES at the surface
 230 Brillouin zone edge⁷ (Figure 4c). Here, we can distinguish the
 231 (100) and (001) surfaces in the ARPES measurement by the
 232 distinct periodicity of the dispersions in momentum space,
 233 which is inversely proportional to the lattice constants a and c
 234 for the (001) and (100) surfaces, respectively.

235 Having eliminated the bulk band and the top/bottom
 236 surface states, we now discuss some non-trivial mechanisms for
 237 the gate-tunable transport in α - Bi_4I_4 . One such channel is the
 238 helical hinge states of α - Bi_4I_4 as a higher order TI³ (panels b
 239 and g of Figure 1). A second possibility is the gapped surface
 240 states on the b - c plane, i.e., on the sides of the device. The
 241 (100) surface state on the b - c plane is seen in our calculated
 242 band structure³ (panels b, c, and f of Figure 1) and in our
 243 ARPES data (panels e-g of Figure 4). Clearly, this (100) side
 244 surface state is a novel 2D electron system with a highly
 245 unusual structure;⁷ while almost dispersionless in the c
 246 direction, it forms a massive Dirac band in the b direction.
 247 As a result of the large spin-orbit coupling and the local
 248 inversion symmetry breaking, the conduction and valence
 249 bands display quasi-1D Rashba-like spin splitting (Figure 1c).

Both the side surface states and the helical hinge states can
 250 contribute to the longitudinal signal and be tunable by V_g ;
 251 however, they should not contribute to the Hall resistance in
 252 our edge-contacted devices. 253

The gate tunable R_{xy} signals therefore suggest the presence
 254 of an additional channel. Here, we consider the last possibility,
 255 which is the 2D TI state that is expected to emerge in
 256 monolayer Bi_4I_4 ⁶ (Figure 1d). On first glance, this possibility is
 257 rather surprising, because our devices are relatively thick. 258
 However, because the interlayer coupling in Bi_4I_4 is extremely
 259 weak (~ 10 meV),⁶ gate-induced charges accumulate primarily
 260 on the bottommost monolayer (or at most 2–3 layers as a
 261 result of screening), similar to that observed in gated bilayer
 262 WSe_2 and MoS_2 .^{37–40} Albeit with a dissimilar dielectric
 263 environment and unrelaxed lattice constants compared to a
 264 freestanding monolayer,²¹ this 2D TI state⁶ hosts a gapped
 265 Dirac cone and, thus, contributes to both R_{xx} and R_{xy}
 266 signals.^{33,34} The absence of conductance quantization is likely
 267 due to the presence of the conductive bulk or the surface/
 268 hinge states. 269

We therefore tentatively attribute the gate-tunable ambipolar
 270 channels to the bottommost 2D TI layer that is effectively
 271 decoupled from the upper layers, the gapped side surface
 272 states, and/or gapless hinge states around the upper layers. All
 273 of these channels are valuable platforms that afford rich
 274 physics, such as mediation of topological superconductivity. As
 275 a demonstration of this possibility, we couple a Bi_4I_4 flake to
 276 Ti/Nb contacts that are separated by ~ 500 nm. Figure 5a
 277 illustrates differential resistance dV/dI versus bias current I and
 278 V_g . Zero resistance states are observed; as I increases at 0.3 K,
 279 at least two pairs of sharp peaks are observed at $\sim \pm 15$ and
 280 $\sim \pm 40$ μA (blue curve of Figure 5b), respectively, correspond-
 281 ing to the critical current I_c values of induced super-
 282 conductivity with $2\Delta_1 \sim 1.2$ meV and $2\Delta_2 \sim 3$ meV, which
 283 are comparable to or less than the superconducting gap of Nb
 284 ($2\Delta_{\text{bulk}} \sim 3$ meV). We note that these critical currents are
 285 considerably larger than those observed in graphene Josephson
 286 junctions with higher mobilities and similar device param-
 287 eters.^{41–44} Because I_c values are tunable by V_g , the supercurrent
 288 must be carried by the gate-tunable channels, consistent with
 289 our proposed mechanism. Moreover, the supercurrent is
 290 completely suppressed at 4.4 K (red curve of Figure 5b) or 291

292 at a critical magnetic field of $H_c \sim 2$ T perpendicular to the a –
293 b plane (Figure 5c). We note that the Fraunhofer pattern is not
294 observed, because it is likely obscured by the supercurrent
295 carried by the conductive bulk and possibly the side surface
296 states. Additional experimental and theoretical investigation
297 will be needed to fully elucidate the magnitude, nature, and
298 mechanism of this exciting gate-tunable proximity-induced
299 superconductivity.

300 In conclusion, we demonstrate gate-tunable transport in α -
301 Bi_4I_4 , which is most consistent with the presence of gapped
302 surface states on the b – c plane, gapless edge states, and/or
303 hinge states around the a – b plane. Emergence of the gate-
304 tunable supercurrent mediated by these states provides a new
305 avenue for creating and manipulating topological super-
306 conductivity and underscores the potential of quasi-1D TIs
307 for realizing the promises of topological materials.

308 ■ ASSOCIATED CONTENT

309 **SI** Supporting Information

310 The Supporting Information is available free of charge at
311 <https://pubs.acs.org/doi/10.1021/acs.nanolett.1c04264>.

312 Details of crystal synthesis, device fabrication, ARPES
313 measurements, and computational methods (PDF)

314 ■ AUTHOR INFORMATION

315 Corresponding Authors

316 **Chun Ning Lau** – Department of Physics, The Ohio State
317 University, Columbus, Ohio 43210, United States;
318 orcid.org/0000-0003-2159-6723; Email: lau.232@osu.edu

320 **Bing Lv** – Department of Physics, The University of Texas at
321 Dallas, Richardson, Texas 75080-3021, United States;
322 orcid.org/0000-0002-9491-5177; Email: blv@utdallas.edu

324 **Fan Zhang** – Department of Physics, The University of Texas
325 at Dallas, Richardson, Texas 75080-3021, United States;
326 orcid.org/0000-0003-4623-4200; Email: zhang@utdallas.edu

328 **Ming Yi** – Department of Physics and Astronomy, Rice
329 University, Houston, Texas 77005, United States;
330 Email: mingyi@rice.edu

331 **Robert J. Birgeneau** – Department of Physics, University of
332 California, Berkeley, Berkeley, California 94720, United
333 States; Email: robertjb@berkeley.edu

334 Authors

335 **Yulu Liu** – Department of Physics, The Ohio State University,
336 Columbus, Ohio 43210, United States

337 **Ruoyu Chen** – Department of Physics, The Ohio State
338 University, Columbus, Ohio 43210, United States;
339 orcid.org/0000-0002-4471-2574

340 **Zheneng Zhang** – Department of Physics, The Ohio State
341 University, Columbus, Ohio 43210, United States

342 **Marc Bockrath** – Department of Physics, The Ohio State
343 University, Columbus, Ohio 43210, United States;
344 orcid.org/0000-0002-7000-1442

345 **Yan-Feng Zhou** – Department of Physics, The University of
346 Texas at Dallas, Richardson, Texas 75080-3021, United
347 States

348 **Chiho Yoon** – Department of Physics, The University of Texas
349 at Dallas, Richardson, Texas 75080-3021, United States;

Department of Physics and Astronomy, Seoul National
University, Seoul 08826, Korea 350–351

Sheng Li – Department of Physics, The University of Texas at
Dallas, Richardson, Texas 75080-3021, United States 352–353

Xiaoyuan Liu – Department of Physics, The University of
Texas at Dallas, Richardson, Texas 75080-3021, United
States 354–356

Nikhil Dhale – Department of Physics, The University of
Texas at Dallas, Richardson, Texas 75080-3021, United
States 357–359

Kenji Watanabe – Research Center for Functional Materials,
National Institute for Materials Science, Tsukuba 305-0044,
Japan; orcid.org/0000-0003-3701-8119 360–362

Takashi Taniguchi – International Center for Materials
Nanoarchitectonics, National Institute for Materials Science,
Tsukuba 305-0044, Japan; orcid.org/0000-0002-1467-3105 363–366

Jianwei Huang – Department of Physics and Astronomy, Rice
University, Houston, Texas 77005, United States 367–368

Ji Seop Oh – Department of Physics, University of California,
Berkeley, Berkeley, California 94720, United States 369–370

Complete contact information is available at: 371
<https://pubs.acs.org/doi/10.1021/acs.nanolett.1c04264> 372

Notes 373

The authors declare no competing financial interest. 374

375 ■ ACKNOWLEDGMENTS

This work is mainly supported by the National Science
Foundation (NSF) through the DMREF program. The work at
The Ohio State University (OSU) is supported by NSF under
Grant DMR-1922076. The work at The University of Texas at
Dallas (UTD) is supported by NSF under Grants DMR-
1921581 and DMR-1945351 and the Army Research Office
(ARO) under Grant W911NF-18-1-0416. The work at Rice is
supported by NSF under Grant DMR-1921847. The work at
the University of California, Berkeley (UCB) is supported by
NSF Grant 1921798. Device fabrication is performed in the
NanoSystems Laboratory (NSL) cleanroom, which is
supported by the Center for Emergent Materials (CEM), a
NSF Materials Research Science and Engineering Center
(MRSEC) (2011876). Sheng Li, Xiaoyuan Liu, Nikhil Dhale,
and Bing Lv also acknowledge the support by the Air Force
Office of Scientific Research (AFOSR) under Grant FA9550-
19-1-0037. Kenji Watanabe and Takashi Taniguchi acknowl-
edge support from the Elemental Strategy Initiative conducted
by the Ministry of Education, Culture, Sports, Science and
Technology (MEXT), Japan, Grant JPMXP0112101001, Japan
Society for the Promotion of Science (JSPS) Grants-in-Aid for
Scientific Research (KAKENHI) Grant JP20H00354, and the
Core Research for Evolutional Science and Technology
(CREST) (JPMJCR15F3), Japan Science and Technology
Agency (JST). Yan-Feng Zhou, Chiho Yoon, and Fan Zhang
acknowledge the Texas Advanced Computing Center (TACC)
for providing resources that have contributed to the research
results reported in this work. 403

404 ■ REFERENCES

- 405 (1) Qi, X.-L.; Zhang, S.-C. Topological insulators and super-
406 conductors. *Rev. Mod. Phys.* **2011**, *83*, 1057. 406
- 407 (2) Hasan, M. Z.; Kane, C. L. Colloquium: Topological insulators.
408 *Rev. Mod. Phys.* **2010**, *82*, 3045. 408

- 409 (3) Liu, C.-C.; Zhou, J.-J.; Yao, Y.; Zhang, F. Weak Topological
410 Insulators and Composite Weyl Semimetals: β -Bi₄X₄ (X = Br, I). *Phys.*
411 *Rev. Lett.* **2016**, *116*, 066801.
- 412 (4) Autès, G.; Isaeva, A.; Moreschini, L.; Johannsen, J. C.; Pisoni, A.;
413 Mori, R.; Zhang, W.; Filatova, T. G.; Kuznetsov, A. N.; Forró, L.; Van
414 den Broek, W.; Kim, Y.; Kim, K. S.; Lanzara, A.; Denlinger, J. D.;
415 Rotenberg, E.; Bostwick, A.; Grioni, M.; Yazyev, O. V. A novel quasi-
416 one-dimensional topological insulator in bismuth iodide β -Bi₄I₄. *Nat.*
417 *Mater.* **2016**, *15*, 154.
- 418 (5) Noguchi, R.; Takahashi, T.; Kuroda, K.; Ochi, M.; Shirasawa, T.;
419 Sakano, M.; Bareille, C.; Nakayama, M.; Watson, M. D.; Yaji, K.;
420 Harasawa, A.; Iwasawa, H.; Dudin, P.; Kim, T. K.; Hoesch, M.;
421 Kandyba, V.; Giampietri, A.; Barinov, A.; Shin, S.; Arita, R.; Sasagawa,
422 T.; Kondo, T. A weak topological insulator state in quasi-one-
423 dimensional bismuth iodide. *Nature* **2019**, *566*, 518.
- 424 (6) Yoon, C.; Liu, C.-C.; Min, H.; Zhang, F. Quasi-One-
425 Dimensional Higher-Order Topological Insulators. *arXiv.org, e-Print*
426 *Arch., Condens. Matter* **2020**, arXiv:2005.14710.
- 427 (7) Huang, J.; Li, S.; Yoon, C.; Oh, J. S.; Wu, H.; Liu, X.; Dhale, N.;
428 Zhou, Y.-F.; Guo, Y.; Zhang, Y.; Hashimoto, M.; Lu, D.; Denlinger, J.;
429 Wang, X.; Lau, C. N.; Birgeneau, R. J.; Zhang, F.; Lv, B.; Yi, M.
430 Room-Temperature Topological Phase Transition in Quasi-One-
431 Dimensional Material Bi₄I₄. *Phys. Rev. X* **2021**, *11*, 031042.
- 432 (8) Noguchi, R.; Kobayashi, M.; Jiang, Z.; Kuroda, K.; Takahashi,
433 T.; Xu, Z.; Lee, D.; Hirayama, M.; Ochi, M.; Shirasawa, T.; Zhang, P.;
434 Lin, C.; Bareille, C.; Sakuragi, S.; Tanaka, H.; Kunisada, S.; Kurokawa,
435 K.; Yaji, K.; Harasawa, A.; Kandyba, V.; Giampietri, A.; Barinov, A.;
436 Kim, T. K.; Cacho, C.; Hashimoto, M.; Lu, D.; Shin, S.; Arita, R.; Lai,
437 K.; Sasagawa, T.; Kondo, T. Evidence for a higher-order topological
438 insulator in a three-dimensional material built from van der Waals
439 stacking of bismuth-halide chains. *Nat. Mater.* **2021**, *20*, 473.
- 440 (9) Ando, Y. Topological Insulator Materials. *J. Phys. Soc. Jpn.* **2013**,
441 *82*, 102001.
- 442 (10) Bansil, A.; Lin, H.; Das, T. Colloquium: Topological band
443 theory. *Rev. Mod. Phys.* **2016**, *88*, 021004.
- 444 (11) Hasan, M. Z.; Xu, S.-Y.; Bian, G. Topological insulators,
445 topological superconductors and Weyl fermion semimetals: Discov-
446 eries, perspectives and outlooks. *Phys. Scr.* **2015**, *2015*, 014001.
- 447 (12) Hsieh, D.; Qian, D.; Wray, L.; Xia, Y.; Hor, Y. S.; Cava, R. J.;
448 Hasan, M. Z. A topological Dirac insulator in a quantum spin Hall
449 phase. *Nature* **2008**, *452*, 970.
- 450 (13) Teo, J. C. Y.; Kane, C. L. Topological defects and gapless
451 modes in insulators and superconductors. *Phys. Rev. B* **2010**, *82*,
452 115120.
- 453 (14) Zhang, H.; Liu, C.-X.; Qi, X.-L.; Dai, X.; Fang, Z.; Zhang, S.-C.
454 Topological insulators in Bi₂Se₃, Bi₂Te₃ and Sb₂Te₃ with a single
455 Dirac cone on the surface. *Nat. Phys.* **2009**, *5*, 438.
- 456 (15) Xia, Y.; Qian, D.; Hsieh, D.; Wray, L.; Pal, A.; Lin, H.; Bansil,
457 A.; Grauer, D.; Hor, Y. S.; Cava, R. J.; Hasan, M. Z. Observation of a
458 large-gap topological-insulator class with a single Dirac cone on the
459 surface. *Nat. Phys.* **2009**, *5*, 398.
- 460 (16) Chen, Y. L.; Analytis, J. G.; Chu, J.-H.; Liu, Z. K.; Mo, S.-K.; Qi,
461 X. L.; Zhang, H. J.; Lu, D. H.; Dai, X.; Fang, Z.; Zhang, S. C.; Fisher,
462 I. R.; Hussain, Z.; Shen, Z.-X. Experimental Realization of a Three-
463 Dimensional Topological Insulator, Bi₂Te₃. *Science* **2009**, *325*, 178.
- 464 (17) Dikarev, E. V.; Popovkin, B. A.; Shevelkov, A. V. New
465 polymolecular bismuth monohalides. Synthesis and crystal structures
466 of Bi₄Br_{4-*x*} (*x* = 1, 2, or 3). *Russian Chemical Bulletin* **2001**, *50*, 2304.
- 467 (18) Filatova, T. G.; Gurin, P. V.; Kloo, L.; Kulbachinskii, V. A.;
468 Kuznetsov, A. N.; Kytin, V. G.; Lindsjo, M.; Popovkin, B. A.
469 Electronic structure, galvanomagnetic and magnetic properties of the
470 bismuth subhalides Bi₄I₄ and Bi₄Br₄. *J. Solid State Chem.* **2007**, *180*,
471 1103.
- 472 (19) von Schnering, H. G.; von Benda, H.; Kalveram, C.
473 Wismutmonojodid Bij, eine Verbindung mit Bi(O) und Bi(II). *Z.*
474 *Anorg. Allg. Chem.* **1978**, *438*, 37.
- 475 (20) Weiz, A.; Anh, M. L.; Kaiser, M.; Rasche, B.; Herrmannsdörfer,
476 T.; Doert, T.; Ruck, M. Optimized Synthesis of the Bismuth
Subiodides Bi_{*m*}I₄ (*m* = 4, 14, 16, 18) and the Electronic Properties
of Bi₁₄I₄ and Bi₁₈I₄. *Eur. J. Inorg. Chem.* **2017**, *2017*, 5609.
- (21) Zhou, J.-J.; Feng, W.; Liu, C.-C.; Guan, S.; Yao, Y. Large-Gap
Quantum Spin Hall Insulator in Single Layer Bismuth Monobromide
Bi₄Br₄. *Nano Lett.* **2014**, *14*, 4767.
- (22) Zhang, T.; Jiang, Y.; Song, Z.; Huang, H.; He, Y.; Fang, Z.;
Weng, H.; Fang, C. Catalogue of topological electronic materials.
Nature **2019**, *566*, 475.
- (23) Vergniory, M. G.; Elcoro, L.; Felser, C.; Regnault, N.; Bernevig,
B. A.; Wang, Z. A complete catalogue of high-quality topological
materials. *Nature* **2019**, *566*, 480.
- (24) Tang, F.; Po, H. C.; Vishwanath, A.; Wan, X. Comprehensive
search for topological materials using symmetry indicators. *Nature*
2019, *566*, 486.
- (25) Halperin, B. I. Possible States for a Three-Dimensional
Electron Gas in a Strong Magnetic Field. *Jpn. J. Appl. Phys.* **1987**,
26, 1913.
- (26) Tang, F.; Ren, Y.; Wang, P.; Zhong, R.; Schneeloch, J.; Yang, S.
A.; Yang, K.; Lee, P. A.; Gu, G.; Qiao, Z.; Zhang, L. Three-
dimensional quantum Hall effect and metal–insulator transition in
ZrTe₅. *Nature* **2019**, *569*, 537.
- (27) Su, W. P.; Schrieffer, J. R.; Heeger, A. J. Solitons in
Polyacetylene. *Phys. Rev. Lett.* **1979**, *42*, 1698.
- (28) Qi, Y.; Shi, W.; Werner, P.; Naumov, P. G.; Schnelle, W.;
Wang, L.; Rana, K. G.; Parkin, S.; Medvedev, S. A.; Yan, B.; Felser, C.
Pressure-induced superconductivity and topological quantum phase
transitions in a quasi-one-dimensional topological insulator: Bi₄I₄. *npj*
Quantum Mater. **2018**, *3*, 4.
- (29) Pisoni, A.; Gaál, R.; Zeugner, A.; Falkowski, V.; Isaeva, A.;
Huppertz, H.; Autès, G.; Yazyev, O. V.; Forró, L. Pressure effect and
superconductivity in the β -Bi₄I₄ topological insulator. *Phys. Rev. B*
2017, *95*, 235149.
- (30) Chen, D.-Y.; Ma, D.-S.; Li, Y.; Du, Z. Z.; Xiong, X.; He, Y.;
Duan, J.; Han, J.; Chen, D.; Xiao, W.; Yao, Y. Quantum transport
properties in single crystals of α -Bi₄I₄. *Phys. Rev. Mater.* **2018**, *2*,
114408.
- (31) Li, X.; Chen, D.; Jin, M.; Ma, D.; Ge, Y.; Sun, J.; Guo, W.; Sun,
H.; Han, J.; Xiao, W.; Duan, J.; Wang, Q.; Liu, C.-C.; Zou, R.; Cheng,
J.; Jin, C.; Zhou, J.; Goodenough, J. B.; Zhu, J.; Yao, Y. Pressure-
induced phase transitions and superconductivity in a quasi-1-
dimensional topological crystalline insulator α -Bi₄Br₄. *Proc. Natl.*
Acad. Sci. **2019**, *116*, 17696.
- (32) Novoselov, K. S.; Geim, A. K.; Morozov, S. V.; Jiang, D.;
Zhang, Y.; Dubonos, S. V.; Grigorieva, I. V.; Firsov, A. A. Electric field
effect in atomically thin carbon films. *Science* **2004**, *306*, 666.
- (33) Brüne, C.; Roth, A.; Buhmann, H.; Hankiewicz, E. M.;
Molenkamp, L. W.; Maciejko, J.; Qi, X.-L.; Zhang, S.-C. Spin
polarization of the quantum spin Hall edge states. *Nat. Phys.* **2012**, *8*,
485.
- (34) Knez, I.; Du, R.-R.; Sullivan, G. Evidence for Helical Edge
Modes in Inverted InAs/GaSb Quantum Wells. *Phys. Rev. Lett.* **2011**,
107, 136603.
- (35) Checkelsky, J. G.; Hor, Y. S.; Cava, R. J.; Ong, N. P. Bulk Band
Gap and Surface State Conduction Observed in Voltage-Tuned
Crystals of the Topological Insulator Bi₂Se₃. *Phys. Rev. Lett.* **2011**,
106, 196801.
- (36) Kim, D.; Cho, S.; Butch, N. P.; Syers, P.; Kirshenbaum, K.;
Adam, S.; Paglione, J.; Fuhrer, M. S. Surface conduction of topological
Dirac electrons in bulk insulating Bi₂Se₃. *Nat. Phys.* **2012**, *8*, 459.
- (37) Fallahazad, B.; Movva, H. C. P.; Kim, K.; Larentis, S.;
Taniguchi, T.; Watanabe, K.; Banerjee, S. K.; Tutuc, E. Shubnikov–de
Haas Oscillations of High-Mobility Holes in Monolayer and Bilayer
WSe₂: Landau Level Degeneracy, Effective Mass, and Negative
Compressibility. *Phys. Rev. Lett.* **2016**, *116*, 086601.
- (38) Movva, H. C. P.; Fallahazad, B.; Kim, K.; Larentis, S.;
Taniguchi, T.; Watanabe, K.; Banerjee, S. K.; Tutuc, E. Density-
Dependent Quantum Hall States and Zeeman Splitting in Monolayer
and Bilayer MoS₂. *Phys. Rev. Lett.* **2017**, *118*, 247701.

- 545 (39) Lin, J.; Han, T.; Piot, B. A.; Wu, Z.; Xu, S.; Long, G.; An, L.;
546 Cheung, P.; Zheng, P.-P.; Plochocka, P.; Dai, X.; Maude, D. K.;
547 Zhang, F.; Wang, N. Determining Interaction Enhanced Valley
548 Susceptibility in Spin-Valley-Locked MoS₂. *Nano Lett.* **2019**, *19*, 1736.
- 549 (40) Pisoni, R.; Davatz, T.; Watanabe, K.; Taniguchi, T.; Ihn, T.;
550 Ensslin, K. Absence of Interlayer Tunnel Coupling of K-Valley
551 Electrons in Bilayer MoS₂. *Phys. Rev. Lett.* **2019**, *123*, 117702.
- 552 (41) Amet, F.; Ke, C. T.; Borzenets, I. V.; Wang, J.; Watanabe, K.;
553 Taniguchi, T.; Deacon, R. S.; Yamamoto, M.; Bomze, Y.; Tarucha, S.;
554 Finkelstein, G. Supercurrent in the quantum Hall regime. *Science*
555 **2016**, *352*, 966.
- 556 (42) Calado, V. E.; Goswami, S.; Nanda, G.; Diez, M.; Akhmerov, A.
557 R.; Watanabe, K.; Taniguchi, T.; Klapwijk, T. M.; Vandersypen, L. M.
558 K. Ballistic Josephson junctions in edge-contacted graphene. *Nat.*
559 *Nanotechnol.* **2015**, *10*, 761.
- 560 (43) Du, X.; Skachko, I.; Andrei, E. Y. Josephson current and
561 multiple Andreev reflections in graphene SNS junctions. *Phys. Rev. B*
562 **2008**, *77*, 184507.
- 563 (44) Ben Shalom, M.; Zhu, M. J.; Fal'ko, V. I.; Mishchenko, A.;
564 Kretinin, A. V.; Novoselov, K. S.; Woods, C. R.; Watanabe, K.;
565 Taniguchi, T.; Geim, A. K.; Prance, J. R. Quantum oscillations of the
566 critical current and high-field superconducting proximity in ballistic
567 graphene. *Nat. Phys.* **2016**, *12*, 318.